

# Inversion of Chromophoric Dissolved Organic Matter From EO-1 Hyperion Imagery for Turbid Estuarine and Coastal Waters

Weining Zhu and Qian Yu

**Abstract**—The significant implication of chromophoric dissolved organic matter (CDOM) for water quality and biogeochemical cycle leads to an increasing need of CDOM monitoring in coastal regions. Current ocean-color algorithms are mostly limited to open-sea water and have high uncertainty when directly applied to turbid coastal waters. This paper presents a semianalytical algorithm, quasi-analytical CDOM algorithm (QAA-CDOM), to invert CDOM absorption from Earth Observing-1 (EO-1) Hyperion satellite images. This algorithm was developed from a widely used ocean-color algorithm QAA and our earlier extension of QAA. The main goal is to improve the algorithm performance for a wide range of water conditions, particularly turbid waters in estuarine and coastal regions. The algorithm development, calibration, and validation were based on our intensive high-resolution underwater measurements, International Ocean Color Coordinating Group synthetic data, and global National Aeronautics and Space Administration Bio-Optical Marine Algorithm Data Set data. The result shows that retrieved CDOM absorption achieved accuracy (root mean square error (RMSE) =  $0.115 \text{ m}^{-1}$  and  $R^2 = 0.73$ ) in the Atchafalaya River plume area. QAA-CDOM is also evaluated for scenarios in three additional study sites, namely, the Mississippi River, Amazon River, and Moreton Bay, where  $a_g(440)$  was in the wide range of  $0.01\text{--}15 \text{ m}^{-1}$ . It resulted in expected CDOM distribution patterns along the river salinity gradient. This study improves the high-resolution observation of CDOM dynamics in river-dominated coastal margins and other coastal environments for the study of land–ocean interactive processes.

**Index Terms**—Chromophoric dissolved organic matter (CDOM), EO-1 Hyperion, ocean color, quasi-analytical algorithm (QAA).

## I. INTRODUCTION

**C**HRMOPHORIC dissolved organic matter (CDOM) is defined as an aquatic organic substance (size  $< 0.2 \text{ }\mu\text{m}$ ) which absorbs ultraviolet and visible light [1]. Due to the tight connection with dissolved organic carbon (DOC), CDOM is

Manuscript received August 26, 2011; revised February 7, 2012, May 23, 2012, July 20, 2012, and September 4, 2012; accepted September 30, 2012. Date of publication November 26, 2012; date of current version May 16, 2013. This work was supported in part by the National Science Foundation under Grant 1025547 and in part by the Office of Naval Research under Grant N000140910346.

W. Zhu was with the Department of Geosciences, University of Massachusetts—Amherst, Amherst, MA 01003 USA. He is now with the Institute for Great Lakes Research and the Department of Geography, Central Michigan University, MI 48858 USA (e-mail: zhu3w@cmich.edu).

Q. Yu is with the Department of Geosciences, University of Massachusetts—Amherst, Amherst, MA 01003 USA (e-mail: qyu@geo.umass.edu).

Color versions of one or more of the figures in this paper are available online at <http://ieeexplore.ieee.org>.

Digital Object Identifier 10.1109/TGRS.2012.2224117

TABLE I  
LIST OF NOTATIONS

Notation	Description
$a(\lambda)$	Absorption coefficient of water (at wavelength $\lambda$ , the same below), including the pure water
$a_t(\lambda)$	Absorption coefficient of water, excluding the pure water
$a_d(\lambda)$	Absorption coefficient of non-algal particles
$a_{dg}(\lambda)$	Absorption coefficient of non-algal particles and CDOM
$a_g(\lambda)$	Absorption coefficient of CDOM
$a_{ph}(\lambda)$	Absorption coefficient of phytoplankton
$b(\lambda)$	Scattering coefficient of water
$b_b(\lambda)$	Backscattering coefficient of water
$b_{bp}(\lambda)$	Backscattering coefficient of particles
$C(\lambda)$	Attenuation coefficient of water
$R_{rs}(\lambda)$	Above-surface remote sensing reflectance
$r_{rs}(\lambda)$	Below-surface remote sensing reflectance

often used as a DOC tracer [2]–[6]. DOC and CDOM are from allochthonous (surrounding terrestrial ecosystem) or autochthonous sources (phytoplankton degradation). In estuary, the former direct inputs of dissolved organic matter from the litter, and decaying of vegetation detritus is dominant; they are transported to estuarine and coastal waters through terrestrial runoff and stream flow [7], [8]. DOC has significant implications on our environment and climate change due to its important role in the carbon cycle [6], [9]–[11]. Studying the concentration and distribution of CDOM in aquatic ecosystems, particularly the estuarine and coastal regions, will greatly improve our understanding of the dynamics of DOC, terrestrial–oceanic carbon cycle, and the impact of anthropogenic activities on water quality.

Remote sensing provides an effective approach to estimate CDOM absorption  $a_g$  (see Table I for the descriptions of notations used in this paper) in a large spatial scope. CDOM, together with chlorophyll and nonalgal particles, changes the underwater light field and consequently influences the water-leaving radiance received by satellite sensors [12]. In recent decades, several inversion algorithms have been developed to estimate CDOM absorption and implemented for a series of *in situ* and satellite sensors, such as Coastal Zone Color Scanner, Sea-viewing Wide Field-of-view Sensor, Moderate Resolution Imaging Spectroradiometer (MODIS), and EO-1 Hyperion [13]–[17]. Some methods are empirical by establishing quantitative relationships between the ratios or functions of remote-sensing reflectance ( $R_{rs}$ ) and  $a_g$  [18]–[22]. Empirical algorithms have demonstrated success in the waters from which data were obtained for algorithm development, but their



performance can degrade substantially when applied to other incompatible waters. This is because the coefficients used in empirical algorithms are derived from data sets that do not necessarily represent all natural variations [23]. On the other hand, semianalytic algorithms, represented by Carder's MODIS [13], Garver–Siegel–Maritorena model [14], [24], linear matrix model [23], [25], [26], and quasi-analytical algorithm (QAA) [27], [28], derive  $a_{dg}(440)$ , the combined absorption of CDOM  $a_g(440)$  and nonalgal particles  $a_d(440)$ , based on specific bio-optical models. The difficulty in partitioning the two components results from their similar absorption spectra. Thus, lumping CDOM and nonalgal particles together limits accurate quantification of CDOM and, consequently, the potentials of establishing a relationship between CDOM and DOC concentrations [29], [30].

Renewed interest in the dynamics of the DOC at the land–ocean interface suggests the need of an improved CDOM inversion method for a wide variety of water types. Most current CDOM algorithms focus on the open-ocean waters or coastal regions of low CDOM concentration with small variation. For example,  $a_g(440)$  is  $\sim 0.005\text{--}0.07\text{ m}^{-1}$  in the Sargasso Sea [7], [30] or  $\sim 0.05\text{ m}^{-1}$  in Chesapeake Bay and Delaware Bay [18]. There is a lack of full examination of these CDOM algorithms on its feasibility in estuaries and river plume, the transition zone between river and ocean environments. This zone is subject to both marine influences (e.g., tides, waves, and the influx of saline water) and riverine influences (e.g., flows of freshwater and sediment). In many typical estuarine and coastal regions, terrigenous CDOM is carried and imported by terrestrial discharge, which could lead to CDOM concentrations two orders of magnitude higher than that in open sea [31], such as that in Atchafalaya Bay ( $a_g(440) \sim 1.5\text{ m}^{-1}$ ). At the same time, nonalgal particles contribute a much greater portion to the total absorption compared to open-ocean waters [32]. Therefore, directly applying algorithms originally designed for use over noncoastal waters to complex coastal waters could generate large uncertainties. For instance,  $R^2$  from an empirical algorithm developed in the U.S. Middle Atlantic Bight dropped from 0.91 to 0.53 when tested by the standard NASA Bio-Optical Marine Algorithm Data Set (NOMAD) [33]. A comparison study by Qin *et al.* [34] also found that the performance of QAA, the algorithm of the best accuracy in retrieving the total absorption among the other seven algorithms in SeaWiFS Data Analysis System, degraded rapidly as water becomes increasingly complex with high CDOM and sediment levels.

The importance of small rivers in the study of CDOM/DOC delivery from landscapes to coasts urges CDOM retrieval at finer spatial resolutions in estuarine and coastal regions compared to current ocean-color products targeted at open oceans. The 1-km resolution of popular ocean-color sensors is too coarse to capture the CDOM details in small estuaries, bays, or river plumes, where the width may only be a few kilometers or even less. In addition, the low spatial resolution produces a large portion of mixed pixels—water pixels are more likely to be contaminated by the features adjacent to or floating on the waters, such as river bank, coastal wetland, vegetation, or boats with a size smaller than the image spatial resolution.

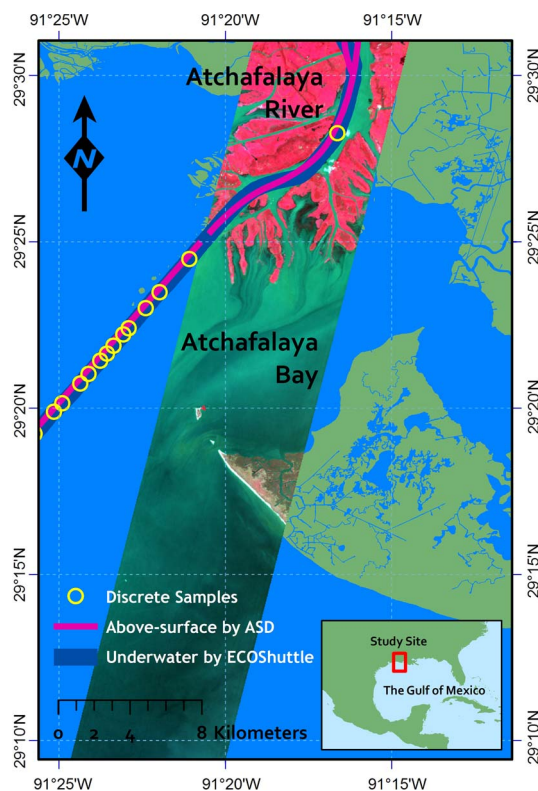


Fig. 1. Cruise tracks and *in situ* measurements in Atchafalaya River estuarine and plume region. The acquired EO-1 Hyperion image covers the same area (Red Green Blue display of Hyperion image uses (R) band 40: 750 nm, (G) band 30: 650 nm, and (B) band 20: 549 nm).

The objectives of this study are to present a new scheme targeting the aforementioned problems and to meet the requirement of CDOM estimation in complex estuarine and coastal regions. This scheme, called QAA-CDOM, is developed from QAA [27], [35] and our recent extension of QAA (QAA-E) to decompose  $a_{dg}$  based on absorption–backscattering relationships [36]. The latter was based on above-surface hyperspectral data and is now extended to the EO-1 Hyperion images. Hyperion imagery has the advantages of continuous band coverage with narrow bandwidth (10 nm) and 30-m spatial resolution. It offers more details in terms of both spectral and spatial domains than current ocean-color sensors. Our scheme has been validated and tested by a number of data sets, including International Ocean Color Coordinating Group (IOCCG) synthetic data, global NOMAD data, and *in situ* high-resolution measurement collected by previous cruises across a variety of geographical sites. In the next sections, we will provide the details of our data collection and processing, field observations, algorithm development and validation, and results from satellite image inversion.

## II. STUDY AREA AND DATA

### A. Study Site

Our main study site is the Atchafalaya River estuarine and plume regions, which cover a transition area of freshwater, fresh–salt-water mixing zone, and salinity water (Fig. 1). The Atchafalaya River is a distributary of the Mississippi and Red



rivers, approximately 270 km long, in south central Louisiana, USA. At the Old River Junction, a man-made system controls the flow of the Mississippi River to the Gulf of Mexico. Seventy percent of the flow drains out of the Birdfoot region through the lower Mississippi River, and 30% is diverted to the Atchafalaya Basin to form the Atchafalaya River [37]. The lower Atchafalaya River flows through wetland, salt marsh and bayou, and the shallow Atchafalaya Bay with a large capacity to trap sediment. It supports a highly productive ecosystem interacting with riverine and estuarine waters, resulting in a substantial CDOM pool [38]–[40].

### B. In Situ Data Acquisition

Our field data collection was conducted during August 24–30, 2007. The *in situ* CDOM concentration and spectral data were measured on the vessel R/V Pelican over the Mississippi and Atchafalaya River plumes, as well as the northern Gulf of Mexico. The major cruise tracks were designed to follow the potential CDOM gradient in the plumes, aiming at capturing the CDOM variations as much as possible (see [36] for the whole study site map and cruise tracks). The data acquisition activities include the following: 1) continuous above-surface hyperspectral measurements [apparent optical properties (AOPs)]; 2) continuous underwater measurements of water attenuation and absorption coefficients [inherent optical properties (IOPs)], salinity, CDOM fluorescence, chlorophyll fluorescence, and optical backscattering for suspended sediments; and 3) discrete water sampling and analysis in laboratory for calibration. The above-surface hyperspectral measurement was conducted by a portable spectroradiometer [Analytical Spectral Devices (ASD) FieldSpec]. The details of the estimation of CDOM using this data set were presented in another paper [36], and this data set was not used in this study.

The underwater measurements were conducted by the ECOShuttle, a towed undulating vehicle based on the Nu-Shuttle manufactured by Chelsea Instruments. The ECOShuttle carries multiple devices, including a SeaTech fluorometer measuring the fluorescent dissolved organic matter. A WET-Labs AC-9 multispectral absorption meter measures the total attenuation and absorption coefficients at nine wavelengths. The spatial resolution of our underwater measurements is very high, and we consequently made a large data set containing about 300 000 samples. In addition, about 150 discrete water samples supplied by ECOShuttle's pumping system were also collected and analyzed to calibrate the real-time underway measurements. Complete details of the ECOShuttle system, discrete sample analysis, field data calibration, and whole study site map and tracks can be referenced from the earlier work done by our team [36], [38], [41], [42].

### C. Satellite Hyperspectral Images

The EO-1 Hyperion cloud-free image of the Atchafalaya River plume regions was requested during fieldtrip date September 4, 2007. We also acquired the image of the Mississippi River plume on August 28, 2007, with 20% cloud cover scattered in the image. Archived images for the Amazon River

estuary (August 22, 2002) and the Moreton Bay in Australia (July 7, 2001) were used as independent sites to test our algorithms. Brando and Dekker have studied the water quality of Moreton Bay and measured its *in situ* CDOM concentration [16]. Their result is served as a reference to evaluate our proposed algorithm.

### D. Standard Data Set for Algorithm Testing

In this paper, the IOCCG synthetic data and NOMAD were used for algorithm analysis and testing. The IOCCG synthetic data consist of 500 water samples with most of the major IOPs (absorption and backscattering coefficients for each ocean-color components) and AOPs ( $R_{rs}$  and  $r_{rs}$ ) based on the HydroLight simulation. NOMAD is an *in situ* data set, which was collected and selected from 515 cruises during 1991–2007 and covering the global oceans. It provides 20 bands between 405 and 683 nm. Detailed descriptions of synthetic data and NOMAD can be found in [23] and [43], as well as in the Web sites of IOCCG and NASA.

## III. METHOD

### A. Image Preprocessing

The raw Level-1G (L1G) EO-1 Hyperion data were pre-processed to retrieve water-leaving remote-sensing reflectance [44], [45]. First, radiometric correction was performed, including abnormal pixel corrections to minimize the problem of periodic line dropouts, line striping, and random noise. Then, atmospheric correction was conducted to compute total reflectance  $R_t$ . Afterward, remote-sensing reflectance  $R_{rs}$  was obtained from  $R_t$  with the aid of HydroLight simulation. Finally,  $R_{rs}$  at four bands required by QAA-CDOM was derived through interpolations.

1) *Atmospheric Correction*: Prior to atmospheric correction, the detector errors were corrected for the L1G Hyperion images, including fixing the random line dropouts, destriping, and noise reduction [45]–[48]. Atmospheric correction was conducted using the Fast Line-of-sight Atmospheric Analysis of Spectral Hypercubes module embedded in ENVI. FLAASH is based on Moderate resolution atmospheric Transmission and a spectral database. It has been fully validated and widely used in hyperspectral remote sensing [49]–[53]. In this paper, correction parameters, such as wind speed (retrieved from National Climate Data Center), aerosol type (maritime), atmospheric model (tropical), and initial visibility (40–60 km), either are from field measurement during cruise [36] or set by the recommended values according to the location and acquisition time of each individual image. In addition, Hyperion's all available bands (426–2500 nm) are used—this assures FLAASH to perform water and aerosol retrievals more accurately. We tested different combinations of these parameters within their reasonable ranges, and we observed no apparent differences among the corrected images. After the correction, the resulted spectra were compared with field measured spectra by ASD. Image spectra exhibit typical water spectral shape. The quality of atmospheric correction was tested



by pairing up and comparing image-derived  $R_t$  and *in situ* above-surface spectra at the same locations. The discrepancy becomes significant at 467 nm (band 12) and shorter. However, the overall quality is good with a mean relative error of  $-1.4\%$  and an RMSE of 0.0063. At the four bands (436, 488, 559, and 641 nm) near those wavelengths used by QAA-CDOM, errors are all below 10%. In addition, the  $F$ -test ensured that field spectra and image-derived spectra are not significantly different for all visible bands (440–700 nm).

2) *Retrieval of Remote-Sensing Reflectance*: Surface reflectance, the reflectance at air–water surface, was removed from the total reflectance to calculate  $R_{rs}$  (remote-sensing reflectance), using [54]

$$R_{rs}(\theta, \varphi) = \frac{R_t}{\pi} - \frac{L_r(\theta, \varphi)}{E_d} \quad (1)$$

where  $R_t$  is the total reflectance at the zenith angle  $\theta$  and azimuth angle  $\varphi$ .  $R_t$  can be obtained by either the direct measurement of ASD [36] or the image output after atmospheric correction. The second term  $L_r(\theta, \varphi)/E_d$ , the ratio of the surface radiance ( $L_r(\theta, \varphi)$ ) to the downwelling irradiance ( $E_d$ ), was simulated by the HydroLight radiative transfer numerical model. The bottom effects were ignored since the water in our study area was reasonably assumed to be optically deep.

3) *Calculating  $R_{rs}$  at Required Wavelengths*: The required bands for calculating  $R_{rs}$  in QAA algorithm were interpolated from the available bands in EO-1 images. The QAA requires  $R_{rs}$  at 440, 490, 555, and 640 nm for the level-1 inversion and  $R_{rs}(410)$  at level 2 for separating  $a_t(440)$  to  $a_{ph}(440)$  (absorption coefficient of phytoplankton pigments) and  $a_{dg}(440)$ . However, the nominal wavelengths of Hyperion bands in the corresponding range are 426, 436, 447, 488, 498, 549, 559, and 641 nm. We determined  $R_{rs\_QAA}$  in the following manner: 1)  $R_{rs\_QAA}(490)$  is linearly interpolated from its adjacent available Hyperion bands at 488 and 498 nm; 2)  $R_{rs\_QAA}(555)$  is linearly interpolated from the bands at 549 and 559 nm; 3)  $R_{rs\_QAA}(640)$  is approximately equal to  $R_{rs\_Hyp}(641)$ ; and 4)  $R_{rs\_QAA}(440)$  is determined by the average of its adjacent bands  $R_{rs\_QAA}(436)$  and  $R_{rs\_QAA}(447)$ . We assigned a lower weight to  $R_{rs\_Hyp}(436)$  than a linear interpolation would do, because the shorter wavelength bands of Hyperion have a lower signal-to-noise ratio. As a result,  $R_{rs}$  required at four bands are given by

$$R_{rs\_QAA}(490) = 0.8R_{rs\_Hyp}(488) + 0.2R_{rs\_Hyp}(498) \quad (2)$$

$$R_{rs\_QAA}(555) = 0.4R_{rs\_Hyp}(549) + 0.6R_{rs\_Hyp}(559) \quad (3)$$

$$R_{rs\_QAA}(640) = R_{rs\_Hyp}(641) \quad (4)$$

$$R_{rs\_QAA}(440) = 0.5R_{rs\_Hyp}(436) + 0.5R_{rs\_Hyp}(447). \quad (5)$$

Note that, since  $R_{rs}(410)$  is not required by our proposed algorithm, we ignore it here.

## B. QAA

Given either  $R_{rs}$  or  $r_{rs}$  as the input, QAA is able to retrieve  $a$ ,  $b_{bp}$  (backscattering coefficient of suspended particles),  $a_{ph}$ , and  $a_{dg}$  at any wavelength. Lee *et al.* [27] proposed this QAA,

which mixes a set of well-known empirical, semianalytical, and analytical models which have been fully studied and validated. Later, Lee *et al.* [35] improved QAA's empirical estimation of  $a(555)$  (the total absorption coefficient), making it more accurate and seamless, and then applied this algorithm to derive euphotic zone depth. QAA does not require prior knowledge of spectral shape of phytoplankton absorption coefficients, and it has already been widely used in ocean-color inversions [23], [55]–[57].

QAA includes three levels, namely, levels 0, 1, and 2; it consists of ten steps. QAA's initial inputs are either  $R_{rs}$  or  $r_{rs}$  at five bands (410, 440, 490, 555, and 640 nm). The outputs at low levels serve as the inputs at high levels. The major products of level 1 are  $a(\lambda)$  and  $b_b(\lambda)$ . At level 2,  $a(\lambda)$  is further separated into  $a_{ph}(\lambda)$  and  $a_{dg}(\lambda)$ . To derive  $a(440)$  from  $R_{rs}(\lambda)$ , QAA (Version 4) executes the following six steps.

Step 0) Estimating  $r_{rs}(\lambda)$

$$r_{rs}(\lambda) = \frac{R_{rs}(\lambda)}{T + \gamma Q R_{rs}(\lambda)} \quad (6)$$

where  $T = 0.52$  and  $\gamma Q = 1.7$ . For CDOM inversion, we need to calculate  $r_{rs}(440)$  and  $r_{rs}(555)$ .

Step 1) Calculating  $u(\lambda)$

$$u(\lambda) = \frac{-g_0 + [(g_0^2 + 4g_1 r_{rs}(\lambda))]^{0.5}}{2g_1} \quad (7)$$

where  $g_0 = 0.0895$ ,  $g_1 = 0.1247$ , and  $u(\lambda)$  is defined by

$$u(\lambda) = \frac{b_b(\lambda)}{a(\lambda) + b_b(\lambda)}. \quad (8)$$

For CDOM inversion, we need to calculate  $u(440)$  and  $u(555)$ .

Step 2) Estimating  $a(555)$

$$a(555) = a_w(555) + 10^{h_0 + h_1 \chi + h_2 \chi^2} \quad (9)$$

with

$$\chi = \log \left( \frac{R_{rs}(440) + R_{rs}(490)}{R_{rs}(555) + 2 \frac{R_{rs}(640)}{R_{rs}(490)} R_{rs}(640)} \right) \quad (10)$$

where  $h_0 = -1.226$ ,  $h_1 = -1.214$ , and  $h_2 = -0.35$ .

Step 3) Calculating  $b_{bp}(555)$

$$b_{bp}(555) = \frac{u(555)a(555)}{1 - u(555)} - b_{bw}(555). \quad (11)$$

Step 4) Calculating  $b_{bp}(440)$

$$b_{bp}(440) = b_{bp}(555) \left( \frac{555}{440} \right)^Y \quad (12)$$

with

$$Y = y_0 \left( 1 - y_1 \exp \left( y_2 \frac{r_{rs}(440)}{r_{rs}(555)} \right) \right) \quad (13)$$

where  $y_0 = 2.2$ ,  $y_1 = 1.2$ , and  $y_2 = -0.9$ .



### Step 5) Calculating $a(440)$

$$a(440) = \frac{(1 - u(440)) (b_{bw}(440) + b_{bp}(440))}{u(440)}. \quad (14)$$

QAA also takes further steps to decompose  $a(440)$  into  $a_{ph}(440)$  and  $a_{dg}(440)$ . Those steps are not included here because they are not used in QAA-CDOM.

### C. QAA-CDOM Algorithm

QAA-CDOM is developed to modify several steps of QAA and QAA-E to improve the algorithm compatibility for complex riverine and estuarine waters. In our earlier study, the QAA-E was developed to retrieve  $a_g(440)$  based on the relationship between  $a_d(440)$  and  $b_{bp}(555)$  or  $a_p(440)$  and  $b_{bp}(555)$  [36], [58], [59]. QAA-E includes two schemes. The  $a_d$ -based scheme decomposes  $a_{dg}(440)$  into  $a_d(440)$  and  $a_g(440)$  using the relationship between  $b_{bp}(555)$  and  $a_d(440)$ . The  $a_p$ -based scheme decomposes  $a_t(440)$  into  $a_p(440)$  and  $a_g(440)$  using the relationship between  $b_{bp}(555)$  and  $a_p(440)$ . The two schemes were compared and validated with two data sets: IOCCG synthetic and our *in situ* spectral data. The results showed that the  $a_p$ -based scheme is slightly better for the *in situ* spectral data and the  $a_d$ -based scheme is slightly better for the IOCCG synthetic data. We choose the  $a_p$ -based scheme for the inversion of satellite images for two reasons. First,  $a_d$ -based QAA-E requires  $R_{rs}(410)$  as input, but this band of Hyperion is not calibrated due to low detector response [60] and also not available for most sensors of similar resolution ( $\sim 30$  m). Second, the  $a_p$ -based scheme can directly return  $a_g(440)$  from the QAA-derived  $a(440)$ , while the  $a_d$ -based scheme needs an intermediate step to decompose  $a(440)$  into  $a_{ph}(440)$  and  $a_{dg}(440)$  and then further partitions  $a_{dg}(440)$  into  $a_d(440)$  and  $a_g(440)$ . In the extra step, some empirical relationships and preset parameters are used, such as CDOM's spectral slope, which inevitably introduces more uncertainties to the final result. Therefore, in this study, we only test the  $a_p$ -based QAA-E.

This new  $a_p$ -based QAA-E algorithm with optimized parameters and functions of QAA is now called QAA-CDOM algorithm. A significant contribution of QAA-CDOM is that some of the equations and coefficients are modified to improve QAA's performance in complex waters using large data sets. We will discuss the details in the next section.

Following QAA's Step 5), to retrieve  $a_g(440)$ , QAA-CDOM continues with the two steps as follows.

### Step 6) Estimating $a_p(440)$

$$a_p(440) = j_1 b_{bp}(555)^{j_2} \quad (15)$$

where  $j_1 = 0.63$  and  $j_2 = 0.88$ . The detail of evaluating the two coefficients is presented in Section IV-C.

### Step 7) Calculating $a_g(440)$

$$a_g(440) = a(440) - a_w(440) - a_p(440). \quad (16)$$

Note that, in the aforementioned equations, the absorption and backscattering coefficients of pure water can be set according to QAA [27].

## IV. RESULTS AND DISCUSSION

### A. *In Situ* IOPs, Ocean-Color Components, and Retrieved $R_{rs}$

The *in situ* IOPs, namely,  $a_t(440)$ ,  $a_t(555)$ ,  $b_{bp}(440)$ , and  $b_{bp}(555)$ , along our track in the Atchafalaya estuary and plume (latitude of 29.1° N–29.55° N) are shown in Fig. 2.  $a_t(440)$  and  $a_t(555)$  were directly measured;  $b_{bp}(440)$  and  $b_{bp}(555)$  were calculated as 2% of the  $b(440)$  and  $b(555)$  [61]; and  $b(440)$  and  $b(555)$  were calculated by  $b(440) = c(440) - a(440)$  and  $b(555) = c(555) - a(555)$ , respectively. The measured absorption coefficients show two facts.

- 1) The total absorption in freshwater and salinity-water mixing area is much higher than that in open-sea water and even higher than that in most of other estuarine and coastal waters presented in the literature. The mean  $a_t(555)$  in the Atchafalaya estuary is around  $0.7 \text{ m}^{-1}$ , which is higher than the maximum  $a_t(555)$  in NOMAD ( $0.6 \text{ m}^{-1}$  observed by only two samples). The measured  $a_t(440)$  is much larger than  $a_t(555)$  [Fig. 2(b)], caused by high CDOM absorptions at short wavelength. The observed  $b_{bp}(440)$  and  $b_{bp}(555)$  are fairly close, indicating suspended sediment-rich water, which has a slow exponential decay of backscattering coefficients toward longer wavelength.
- 2) The IOPs in the Atchafalaya River mouth have large variability and complicated spatial distribution. For example,  $a_t(555)$  between 29.3° N and 29.5° N is in the range of  $0.4$ – $1.5 \text{ m}^{-1}$  [Fig. 2(a)]. The broad range of the absorption coefficients is consistent with other visible bands, for example,  $a_t(440)$  shown in Fig. 2(c4). This high variability corresponded to the gradient of the ratio of freshwater to salinity water.

The field measurement reveals that three major ocean-color components, namely, nonalgal particles (represented by turbidity in unit of Formazin Turbidity Unit (FTU)), chlorophyll ( $\text{mg}/\text{m}^3$ ), and CDOM ( $\text{m}^{-1}$ ), vary independently from one another along Atchafalaya plume [Fig. 2(c)]. Overall, CDOM shows a smooth decrease along the salinity ascending gradient. This monotonic change confirms that CDOM distribution is terrestrial driven. Freshwater input from surrounding watersheds contributes dominantly over new CDOM production from *in situ* biologic activity. Unlike CDOM, chlorophyll has several local maxima and minima, which indicates that local phytoplankton biomass production contributes to the level of chlorophyll. The influence of local environmental conditions to the level of nonalgal particles represented by turbidity is even more abrupt, due to coastal and river morphology, tributaries converging, even boat traffics, etc. In the region 29.20° N–29.26° N, CDOM and  $a_t(440)$  both steadily rise, whereas nonalgal particles and chlorophyll show more fluctuation. This indicates that CDOM is the main contributor to  $a_t(440)$ . However, closer to the river channel, the impact of nonalgal particles on the total absorption coefficient increases, according to the covariation of turbidity and  $a_t(440)$ .

The scattering and absorption of the three optically significant in-water components determined the water-leaving radiance. Fig. 2(d) plots the  $R_{rs}$  retrieved from Hyperion image at four bands (440, 490, 555, and 640 nm) along the cruise



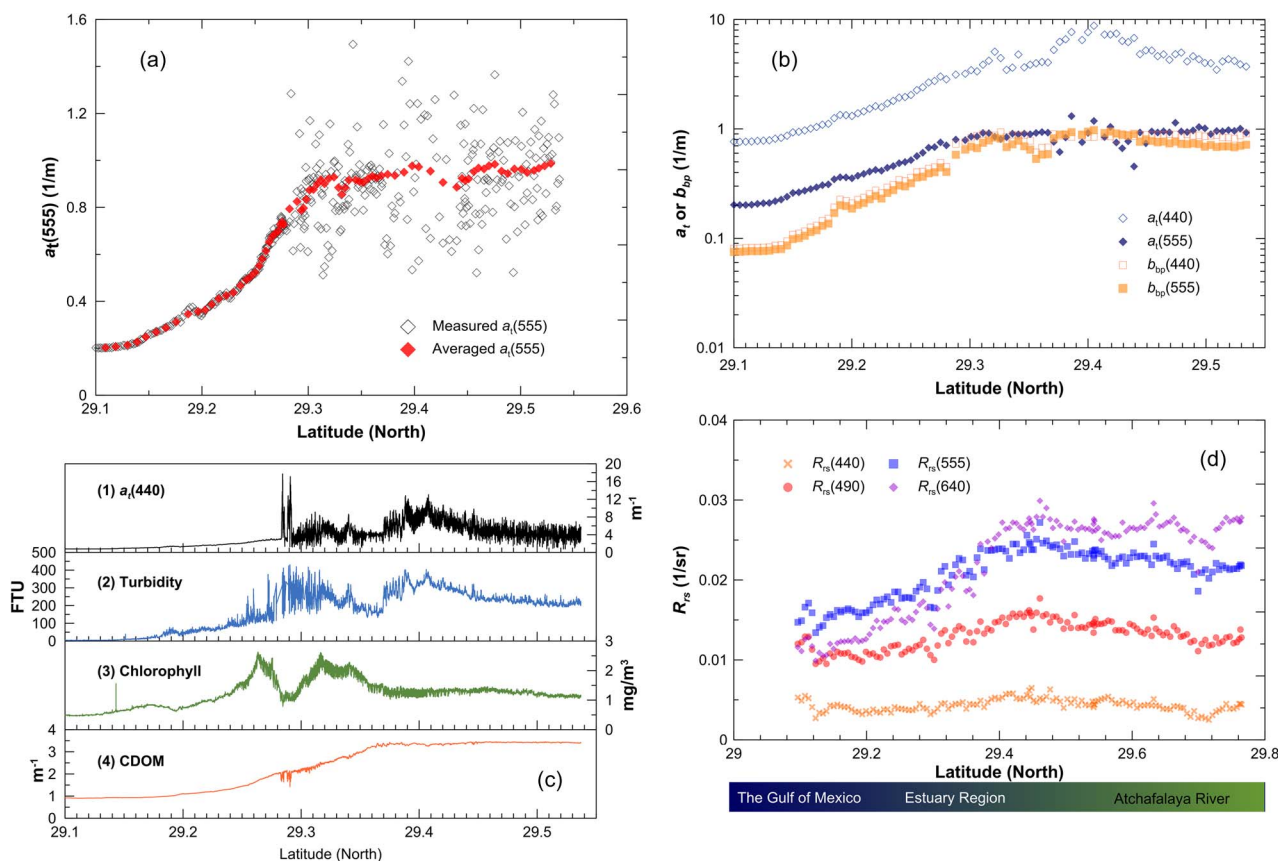


Fig. 2. *In situ* measured and remotely sensed data along the Atchafalaya estuary and plume. (a) Original data of  $a_t(555)$ . (b)  $a_t(440)$ ,  $a_t(555)$ ,  $b_{bp}(440)$ , and  $b_{bp}(555)$ , smoothed by median for each 0.001 latitude degree ( $\sim 90$  m). (c) Concentrations of ocean-color components (original without smoothing): (c1)  $a_t(440)$  ( $\text{m}^{-1}$ ); (c2) sediments (FTU); (c3) chlorophyll ( $\text{mg}/\text{m}^3$ ); (c4) CDOM ( $\text{m}^{-1}$ ). (d) Remote-sensing reflectance (four bands, namely, 440, 490, 555, and 640 nm, used by QAA-CDOM retrieved from the EO-1 Hyperion image).

line in Atchafalaya River estuary and plume. The trend of each band, low in the plume and high in the river, is similar to the observations of IOPs and ocean-color components. The crossing of  $R_{rs}(555)$  and  $R_{rs}(640)$  at the river mouth could be caused by various reasons, for instance, the chlorophyll or nonalgal particle maximum occurred. In fact, the chlorophyll maximum was observed in Fig. 2(c). The chlorophyll and nonalgal particles of high concentrations and spatial variation in turbid estuarine regions make accurate CDOM inversion from water-leaving radiance difficult.

### B. Optimization of QAA for Coastal Waters

We evaluated QAA presented in (6)–(14) step by step and modified some of the steps to minimize the CDOM estimation uncertainty for coastal waters.

1) *Evaluation of  $r_{rs}$* : At Step 0) of QAA,  $r_{rs}$  is estimated from (6) with two parameters. One is  $T = t_- t_+ / n^2$ , and the other is  $\gamma Q$ , where  $t_-$  is the radiance transmittance from below to above the surface,  $t_+$  is the irradiance transmittance from above to below the surface,  $n$  is the refractive index of water,  $\gamma$  is the water-to-air internal reflection coefficient, and  $Q$  is the ratio of upwelling irradiance to upwelling radiance evaluated below the surface. QAA suggests  $T \approx 0.52$  and  $\gamma Q \approx 1.7$  based on HydroLight simulation. In this paper, we refit  $R_{rs}$  and  $r_{rs}$  using IOCCG synthetic data ( $r_{rs}$  is not available in our field

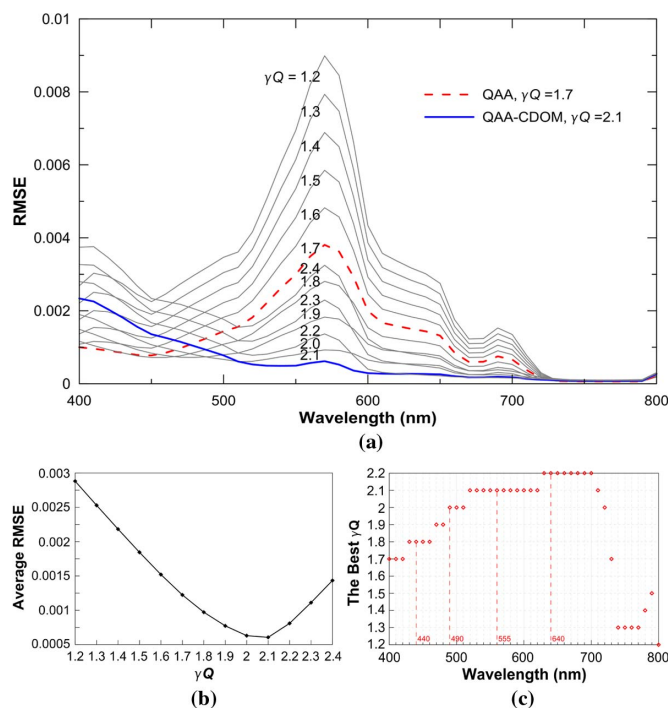


Fig. 3. Adjustment of  $\gamma Q$  used for predicting  $r_{rs}$  from  $R_{rs}$ , using IOCCG synthetic data. (a) RMSE between true and derived  $r_{rs}$  with different  $\gamma Q$  from 1.2 to 2.4. (b) RMSE averaged over 400–800 nm for each  $\gamma Q$ . (c) Best  $\gamma Q$  for each wavelength.



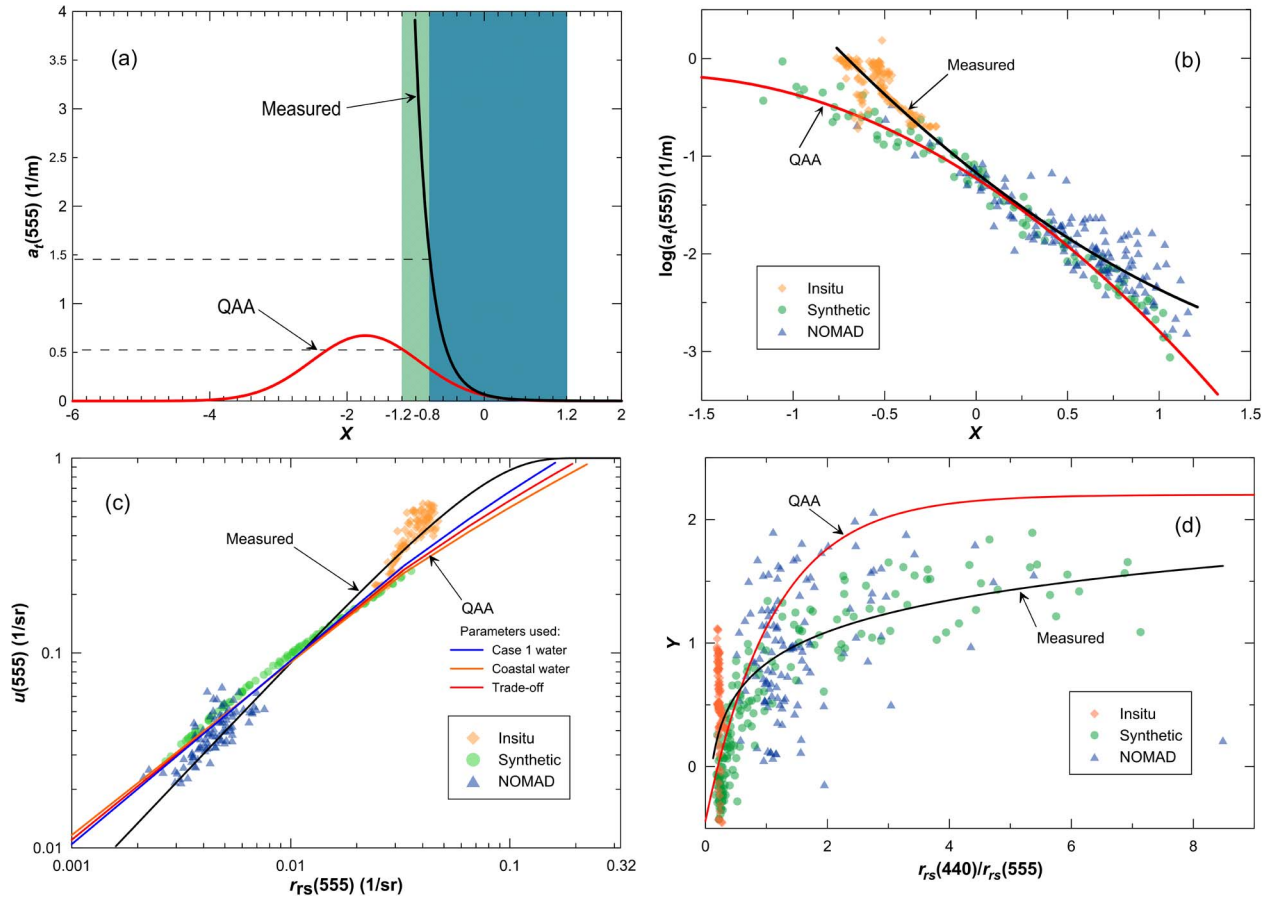


Fig. 4. Optimization of QAA. (a) Graphs of the functions for estimating  $a_t(555)$ . The red one uses QAA's original coefficients, and the black uses the new coefficients by fitting measured data [see (b)]. (b) Adjustment of  $h_0$ ,  $h_1$ , and  $h_2$  to estimate  $a_t(555)$  from  $\chi$ , by fitting IOCCG synthetic data, our *in situ* data, and NOMAD data sets. The new polynomial coefficients are  $h_0 = -1.169$ ,  $h_1 = -1.468$ , and  $h_2 = 0.273$  with  $R^2 = 0.94$ . (c) Adjustment of the relationship between  $r_{rs}$  and  $u$ . New equation is suggested by (18), by fitting all three data sets, with  $R^2 = 0.92$ . The three QAA's curves are generated by using different parameters:  $g_0 = 0.0949$  and  $g_1 = 0.0794$  for case 1 water,  $g_0 = 0.084$  and  $g_1 = 0.17$  for coastal water, and  $g_0 = 0.0895$  and  $g_1 = 0.1274$  for the tradeoff. (d) Adjustment of power decay between backscattering coefficients  $b_{bp}(440)$  and  $b_{bp}(555)$ .

data and NOMAD), and we found that  $T \approx 0.52$  does return the lowest RMSE, but a better value for  $\gamma Q$  is 2.1. Fig. 3(a) shows the RMSE of predicted  $r_{rs}$  across the wavelength varies with  $\gamma Q$  (from 1.2 to 2.4). When  $\gamma Q$  is as low as 1.2, RMSE at the range of 450–650 nm is much higher than those at shorter wavelength ( $< 450$  nm) and longer wavelength ( $> 650$  nm), indicating that a given  $\gamma Q$  gives rise to different errors at different wavelengths. If we use the average RMSE of all wavelengths (400–800 nm) to evaluate  $\gamma Q$ , then  $\gamma Q = 2.1$  has the lowest mean RMSE [Fig. 3(b)], i.e., the estimated  $r_{rs}$  is closest to true  $r_{rs}$ . Therefore, for converting  $R_{rs}$  to  $r_{rs}$ , we suggest keeping the value of  $T$  as in QAA but adjusting  $\gamma Q$  to 2.1 to guarantee the least error for  $r_{rs}$  across 400–800 nm. More accurately, the best  $\gamma Q$  can be identified for each individual wavelength as shown in Fig. 3(c). Specifically, for the four bands (440, 490, 555, and 640 nm) used in QAA-CDOM, the best  $\gamma Q$  values are 1.8, 2.0, 2.1, and 2.2, respectively.

2) *Calibrating  $a_t(555)$ ,  $u(555)$ , and  $b_{bp}(440)$* : At QAA's third step,  $a(555)$ , which is empirically derived from (9), is a critical variable. It is the basis for deriving other IOPs. Given that  $a_t = a - a_w$ , (9) turns to

$$a_t(555) = 10^{h_0 + h_1 \chi + h_2 \chi^2}. \quad (17)$$

Substituting  $h_0 = -1.226$ ,  $h_1 = -1.214$ , and  $h_2 = -0.35$  as suggested by QAA, it is easy to find that (17) reaches its maximum 0.67 as  $\chi$  approaches  $-1.734$  [Fig. 4(a)]. That is to say, the maximum  $a_t(555)$  that can be derived from QAA is  $0.67 \text{ m}^{-1}$ . In practice, even 0.67 is unlikely to be reached, because a value of  $\chi = -1.734$  is almost impossible in real natural waters. The range of  $\chi$  based on IOCCG synthetic data is from  $-1.2$  to  $1.2$  [line-filled area in Fig. 4(a)]. To obtain  $\chi = -1.734$  in (10), the required combinations of the four  $R_{rs}$  are beyond the observed spectral range of natural waters. The range of  $\chi$  based on NOMAD and our *in situ* data set together (referred to as field data hereafter) is  $-0.8$ – $1.2$ . In this range, the maximum  $a_t(555)$  returned by QAA is only about 0.3. This value is much less than the field measured  $a_t(555)$  in our study site, particularly for extremely complex water in estuarine and coastal regions. For instance, in the Atchafalaya mouth and plumes,  $a_t(555)$  has an average of  $1.0 \text{ m}^{-1}$  and sometimes even reaches values greater than  $2.0 \text{ m}^{-1}$ .

The three coefficients used by QAAs (17) were derived from synthetic data only. Three data sets, namely, the IOCCG synthetic data, NOMAD, and our *in situ* data, are aggregated in Fig. 4(b). The sample dots illustrate the discrepancy between synthetic data and field measurement data with respect to the



$a_t(555) - \chi$  relationship. Based on those results, we recalibrated the  $a_t(555) - \chi$  relationship using all three data sets. The coefficients are adjusted to  $h_0 = -1.169$ ,  $h_1 = -1.468$ , and  $h_2 = 0.274$ , plotted as a black line. The original QAA function fits IOCCG synthetic data well (plotted as an orange line) where  $\chi$  is in the middle of the range at around zero, but it underestimates  $a_t(555)$  when  $\chi$  is either small (in NOMAD) or large (in *in situ* data). Using the three new coefficients, there is no limit for the maximum  $a_t(555)$  retrieved from (17), but in the field-observed range of  $\chi$  between  $-0.8$  and  $1.2$ , the maximum  $a_t(555)$  is about  $1.5 \text{ m}^{-1}$  [Fig. 4(a)]. Although we could not validate the cases with  $\chi < -0.8$ , currently, our new coefficient set is the best for the known field data of a reasonably large range.

Next, we evaluate how well  $u(555)$  is predicted from  $r_{rs}(555)$  by (7) in QAA. QAA uses a second-degree polynomial function,  $r_{rs} = g_0u + g_1u^2$ , to describe the relationship between  $u$  and  $r_{rs}$ . This function was originally obtained by least squares regression of Monte Carlo simulated data [62] and works generally well for modest water cases. However, we found that it only fits the simulated data (IOCCG synthetic) well but poorly if we aggregate all three data sets together, particularly for those measured data sets (NOMAD and our *in situ*), so a new finer function is proposed to describe all data sets

$$u(\lambda) = 1 - \exp\left(\frac{-k_0 r_{rs}(\lambda)^{k_1}}{0.31 - r_{rs}(\lambda)}\right) \quad (18)$$

where  $0.31 \approx 1/\pi$  is the idealized maximum of  $r_{rs}$  in the extreme case that almost all incident irradiance is reflected [63], and  $k_0$  and  $k_1$  are two new coefficients to replace  $g_0$  and  $g_1$ , respectively. We can imagine water in this case as very shallow with bottom albedo close to one. For deep and extremely turbid water, we can imagine two ideal cases. First, water is extremely turbid containing perfect “white” particles with  $b_b$  being much greater than  $a$ , and hence,  $u = b_b/(a + b_b)$  approaches one resulting in  $r_{rs} = 1/\pi$ . Second, water is extremely turbid containing perfect “black” particles with  $a$  being very high and much greater than  $b_b$ , and  $u = b_b/(a + b_b)$  approaches zero resulting in  $r_{rs} = 0$ . Equation (18) guarantees the aforementioned two boundary cases, so it is more robust than the QAA. In QAA, when  $r_{rs}$  is close to  $0.31$ , QAA’s function generates an invalid  $u$ , greater than one. Fitting (18) with the three entire data sets (synthetic, NOMAD, and our field data) gives  $k_0 = 6.807$  and  $k_1 = 1.186$  with  $R^2 = 0.92$  [Fig. 4(c)]. Note that  $g_0$  and  $g_1$  used by QAA actually are the tradeoff between oceanic case 1 water and coastal water. Their values are from the average of Gordon’s values for case 1 water ( $g_0 = 0.0949$  and  $g_1 = 0.0794$ ) and Lee’s values for coastal water ( $g_0 = 0.084$  and  $g_1 = 0.17$ ) [27]. We also tested the two original parameter sets. The relationships between  $u(555)$  and  $r_{rs}(555)$  described by all three parameter sets are similar. They only fit the IOCCG synthetic data well but do not fit the *in situ* data (NOMAD and our *in situ*) as well as our proposed (18).

We then assessed the accuracy of the inverted  $b_{bp}(440)$  values, which are calculated from the power function of backscattering coefficients as expressed in (12). Based on the measured

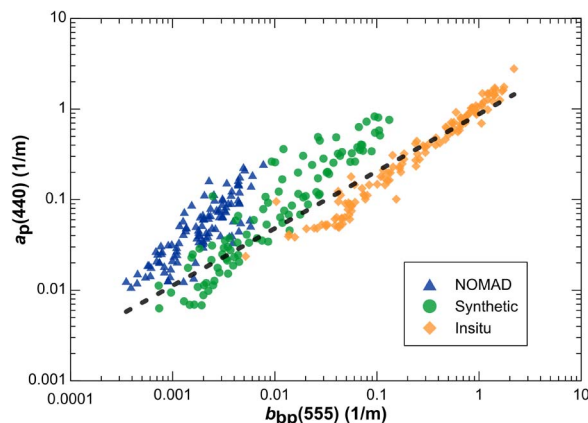


Fig. 5. Relationships between  $b_{bp}(555)$  and  $a_p(440)$ . New fitting between  $b_{bp}(555)$  and  $a_p(440)$  combines the three data sets with  $R^2 = 0.88$ , with  $j_1 = 0.63$  and  $j_2 = 0.88$ .

$b_{bp}(440)$  and  $b_{bp}(555)$ , the relationship between the measured  $Y$ , calculated by  $Y = \log(b_{bp}(440)/b_{bp}(555)) / \log(555/440)$ , and  $r_{rs}(440)/r_{rs}(555)$  is plotted in Fig. 4(d). As  $r_{rs}(440)/r_{rs}(555)$  increases,  $Y$  trends toward 1.9, instead of 2.2, as QAAs predicted. However, for turbid waters such as that in the Atchafalaya River, the range of measured  $r_{rs}(440)/r_{rs}(555)$  is quite narrow within 0.2–0.4, and the results are not sensitive to the parameter  $Y$ . Given that  $Y$  is a power of the base ( $555/440 = 1.26$ ),  $Y$  will not lead to a big difference in the calculation of  $b_{bp}(440)$ . Moreover,  $Y$  is listed as the second-order importance in QAA [27], and we decided to keep QAA’s (13) and its coefficients unchanged in QAA-CDOM.

### C. Inversion of $a_g(440)$ With QAA-CDOM

The key step of the  $a(440)$  decomposition is to examine the relationship of  $a_p(440)$  versus  $b_{bp}(555)$  and determine the two coefficients  $j_1$  and  $j_2$ . The suggested values based on synthetic and our *in situ* data were given in (15) [36]. Here, we added the NOMAD to the previous data set to verify these relationships and refit their coefficients. Fig. 5 shows that all  $a_p(440)$  and  $b_{bp}(555)$  are well correlated—they have similar slopes  $j_1$ , but the interception  $j_2$  shifted ( $R^2 = 0.88$ ). Since we have shown that  $j_1$  and  $j_2$  are not of primary importance, we made an approximate fitting with respect to the three data sets and then established the  $a_p - b_{bp}$  relationship in QAA-CDOM as (15). The equation satisfies our previous conclusion that  $j_1$  and  $j_2$  are not sensitive to the final  $a_g(440)$  prediction when  $0.5 < j_1 < 8.5$  and  $0.8 < j_2 < 2.0$  [36].

$a_g(440)$  was inverted from EO-1 Hyperion image by (16) using the aforementioned calibrated intermediate variables. The inversion result clearly shows the expected distribution and gradient of CDOM from the lower Atchafalaya River channels (latitude of  $29.48^\circ \text{ N}$ ) to Atchafalaya estuarine and plume regions (latitude of  $29.1^\circ \text{ N}$ ) [Fig. 6(a)]. CDOM is high, close to inland Morgan City, LA. The high CDOM maintains through the estuarine wetland and then started decreasing toward the bay. The lowest CDOM occurs at the end of the plume. The image captured broadly ranged CDOM concentrations from



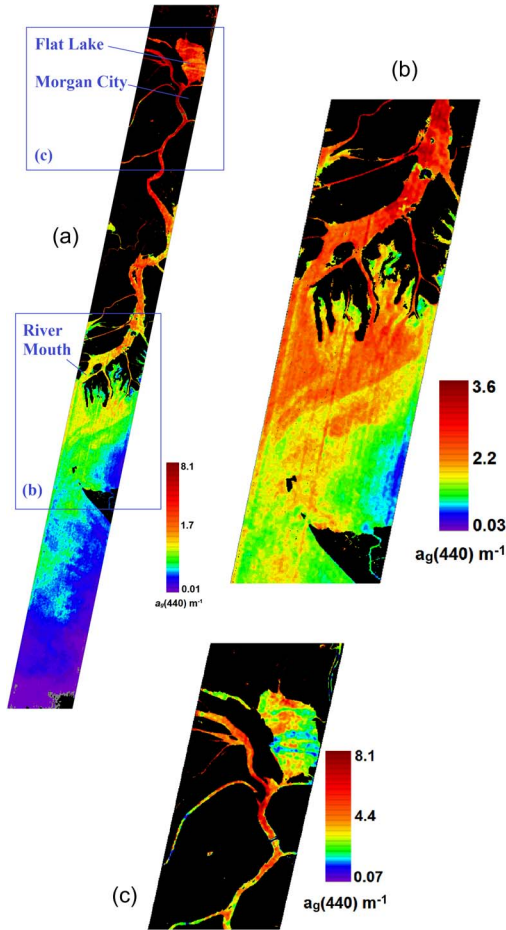


Fig. 6. Spatial distribution of  $a_g(440)$  in Atchafalaya estuary and plume regions. (a) Whole scene. (b) River mouth. (c) Morgan City and Flat Lake. Note that the results are smoothed by a  $3 \times 3$  mean window.

$0.01 \text{ m}^{-1}$  (at the far end of the plume) to  $8.2 \text{ m}^{-1}$  (in inland river water).

Fig. 6(b) and (c) shows the same image zoomed in the channel at the river mouth and near Morgan City to show detailed gradients. In the mouth region,  $a_g(440)$  varies from  $0.05$  to  $3.5 \text{ m}^{-1}$ . An apparent decrease of  $a_g(440)$  across the plume direction is due to the seawater of low CDOM concentration from Fourleague Bay (in the west of the river mouth) intruding into the CDOM-rich freshwater from the river. The CDOM inversion around Morgan City is also consistent with the measurements [Fig. 6(c)]. At upper Morgan City, the six-mile lake through Stouts Pass and the Flat Lake through the Drews Pass merge into the lower Atchafalaya River, carrying a large amount of CDOM originated from nearby wetland ecosystem. As a result,  $a_g(440)$  in the main channel below the merging point was relatively higher than those in waters at either the upper river or the lake. When the river passed by Morgan City, the  $a_g(440)$  decreased slightly due to the low CDOM production in urban area and degradation of the existing CDOM loading. The CDOM absorption in Flat Lake shows an irregular pattern which might be caused by autochthonous sources, such as floating or subsurface algal there. The image was acquired in summer, when the algal is productive in lentic water (lakes or impoundments).

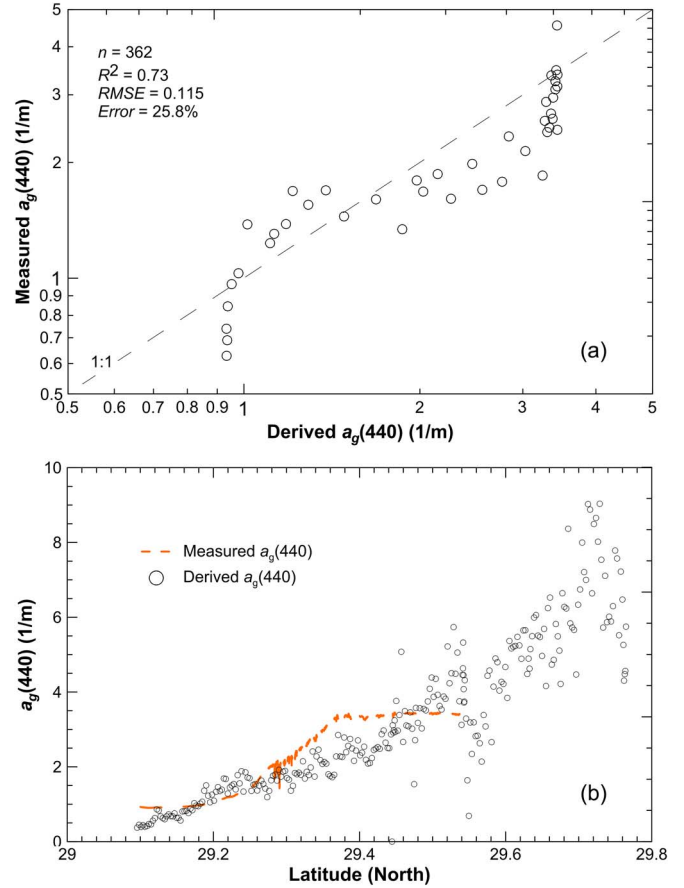


Fig. 7. Validation of QAA-CDOM in the Atchafalaya River estuary and plume regions. (a) Comparison between QAA-CDOM-derived CDOM and measured CDOM. (b) The same comparison but along the cruise track.

#### D. Validation and Uncertainties

Fig. 7(a) plots the inversion-derived  $a_g(440)$  versus the measured one. The accuracy is evaluated by RMSE and error calculated from the following two equations:

RMSE

$$= \left( \frac{1}{n-2} \sum_{i=1}^n [\log(a_{g1}(440)_i) - \log(a_{g2}(440)_i)]^2 \right)^{0.5} \quad (19)$$

error

$$= \left( \frac{1}{n} \sum_{i=1}^n \frac{|a_g(440)_i^{\text{Derived}} - a_g(440)_i^{\text{Measured}}|}{a_g(440)_i^{\text{Measured}}} \right) \times 100\%. \quad (20)$$

In (19),  $a_{g1}$  and  $a_{g2}$  are derived  $a_g(440)$  and measured  $a_g(440)$ , respectively. Within an image pixel ( $30 \text{ m} \times 30 \text{ m}$ ), there were approximately 10–50 *in situ* data points measured, depending on the instrument setting and vessel speed at that time. All *in situ* measures within this pixel are averaged as the ground truth corresponding to the pixel. We then derived  $RMSE = 0.115$  and  $error = 25.8\%$  for  $n = 362$  samples. To observe the association of estimation discrepancy and location, Fig. 7(b) plots measured and retrieved CDOMs along our cruise



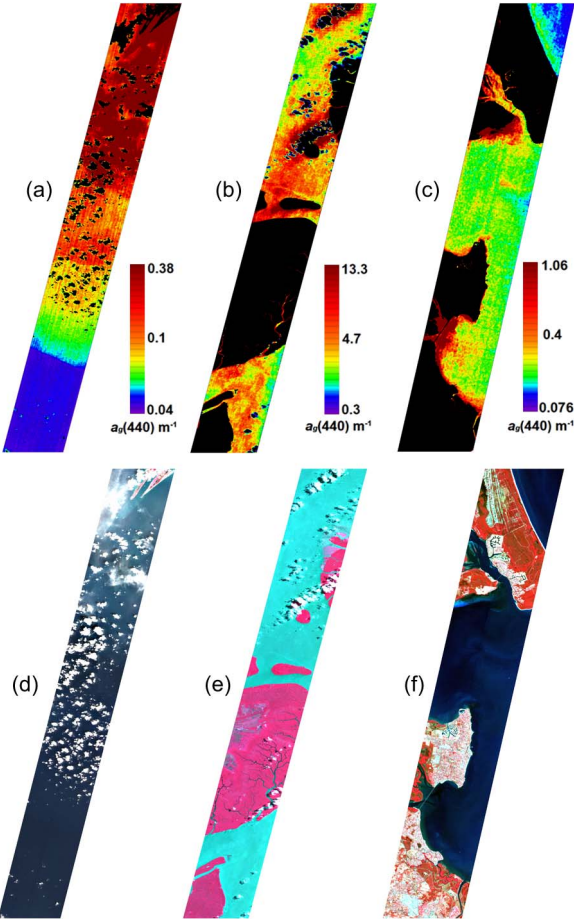


Fig. 8. Spatial distributions of  $a_g(440)$  in three sites: (a) Mississippi River plume, (b) Amazon estuary, and (c) Moreton Bay. Note that black areas are nonwater features—being either land or cloud. (d)–(f) Their respective Hyperion pseudocolor images.

TABLE II  
COMPARISON OF DERIVED AND MEASURED  $a_g(440)$   
(IN PER METER) IN FOUR SITES

Site	Derived			Measured		
	Min	Mean	Max	Min	Mean	Max
Atchafalaya	0.6	1.4	4	0.8	1.62	3.6
Mississippi	0.04	0.08	0.4	0.07	0.11	0.6
Amazon	1.8	4.2	8.6	N/A	~3.8	N/A
Moreton Bay	0.15	0.45	0.8	0.13	N/A	0.75

track in the Atchafalaya River and plume, decreasing from 4 to  $0.6\text{ m}^{-1}$  toward downstream. The inversion result shows the same general trend as *in situ* measurement. Compare with the ground truth, the derived CDOM was slightly underestimated in estuarine area ( $\sim 29.3^\circ\text{ N}$ – $29.4^\circ\text{ N}$ ). This is likely due to the complex mixture with chlorophyll and nonalgal particle mixture in this region [see Fig. 2(c)]. The spatially dramatic change of in-water optical constituents and the lack of covariation between them lead to uncertainty in CDOM estimation. Other uncertainties may come from bottom effect and QAA algorithm itself [64], and therefore, we need to carefully treat the water that is very close to banks or coasts.

QAA-CDOM was also tested for low-CDOM waters ( $a_g(440) < 1\text{ m}^{-1}$ ) by using IOCCG synthetic and NOMAD data. The results ( $\text{RMSE} = 0.38$  and  $R^2 = 0.72$ ) indicate that

it works well for those low-CDOM waters which usually occur in open sea. The QAA-CDOM algorithm was further applied to three other regions, namely, the Mississippi River plume, the Amazon River estuary, and Moreton Bay. The inverted  $a_g(440)$  was evaluated by the distribution pattern and value ranges, see Fig. 8 and Table II. In the area from the far end of river mouth to the open sea, which coincides with our cruise track, the measured CDOM varies from  $0.07$  to  $0.6\text{ m}^{-1}$ , while the image-derived  $a_g(440)$  is about  $0.04$ – $0.4\text{ m}^{-1}$ . These values are quite close. The inverted  $a_g(440)$  in the Amazon River estuary is in the range of  $2$ – $8\text{ m}^{-1}$ , and some extremes may reach  $13\text{ m}^{-1}$ . We did not collect *in situ* data in this site, and the result was compared with published field measurements in the Amazon area [65], [66] in Table II and satellite products of the Coast-Colour Project ([http://www.coastcolour.org/site\\_21.html](http://www.coastcolour.org/site_21.html)). The mean of inverted CDOM is close to the field measurement, and the gradient and range are coincident with published Medium Resolution Imaging Spectrometer (MERIS) inversion. The region of the Amazon River estuary is near the equator and flows mostly through tropical rainforests. The vegetation coverage of its watershed is greater and denser than that of the Atchafalaya River, and consequently, CDOM concentrations in the Amazon are expected to be greater than those in the Atchafalaya in the same season (both EO-1 images are collected in summer). The results of inverted  $a_g(440)$  concurred with this expectation. The results in Moreton Bay also fall within a sensible range. According to published field measurements [16], CDOM in this bay ranges from  $0.13$  to  $0.75\text{ m}^{-1}$ . CDOM that was retrieved by QAA-CDOM ranges from  $0.15$  to  $0.8\text{ m}^{-1}$ . The measured CDOM in January and that derived in July are from different seasons, which can lead to the discrepancy on field CDOM. However, because Moreton Bay is very close to tropic with only  $10^\circ\text{ C}$  dropping from January to July, vegetation there is almost subtropical evergreen. In addition, the river discharge around this bay is low and also varies little due to steady precipitation. It is reasonable to assume that CDOM in this bay area would not vary significantly. Moreover, our results reveal a wider variation of  $a_g(440)$  in this larger area. For example, at the image upper right corner, CDOM in seawater is as low as  $0.07\text{ m}^{-1}$ , while at the lower left corner in the mouth of North Pine River, CDOM is apparently higher than that in the bay. The previous CDOM inversion by Brando and Dekker (2003) used matrix inversion method (MIM) algorithm and encountered some negative  $a_g(440)$  in the resultant images. This implies that the MIM method, or some of its coefficients, may not be suitable for retrieving CDOM in relatively deep clear water, while QAA-CDOM overcome this problem and resulted in all positive  $a_g(440)$  values. Due to a calibration based on a wide range of CDOM absorption, QAA-CDOM is reasonably robust with both CDOM-rich and CDOM-poor water.

V. SUMMARY AND CONCLUSION

Our *in situ* measurements, satellite images, and algorithm development have been focused on estuaries and river-dominated coastal margins where bio-optical and biogeochemical properties are more complex than those in other coastal regions and open-sea waters. The complexity is due to large freshwater



input and freshwater/salinity-water interaction. We conclude our findings in four major aspects: 1) complexity of CDOM distribution pattern in estuarine water; 2) challenges to current ocean-color algorithms; 3) highlights of QAA-CDOM inversion algorithm; and 4) advantages and concerns of using Hyperion satellite images for studying river ecology.

First, high-resolution *in situ* measurements are necessary to map and to understand the spatial variations of the major ocean-color components CDOM, phytoplankton, and nonalgal particles in estuarine water and river plume areas. The CDOM spatial distribution changes according to complex hydrodynamics in lotic river systems and various sources controlled by the drainage watershed characteristics, such as wetland areas and vegetation type and density, and tidal interactions. The range of CDOM concentrations could be two orders of magnitude broader than that in open seas. The dramatic changes of CDOM from freshwater to salinity water along rivers and river plumes convinced the advantages of using the high-resolution *in situ* measurements over stationary IOP observation, particularly for the purpose of developing or validating new ocean-color inversion algorithms.

Second, the decomposition of  $a_{dg}$  so as to derive CDOM absorption ( $a_g$ ) is a critical procedure for estuary water which has a high level of spectral interferences from chlorophyll and sediments. The proposed QAA-CDOM algorithm partitions  $a_t$  to  $a_g$  and  $a_p$  using a semianalytical absorption-scattering relationship. The algorithm development relied on our intensive high-resolution *in situ* bio-optical measurement in river plume area and extensive global ocean-color validation data sets. In the Atchafalaya river region, the CDOM inversion with an EO-1 Hyperion image achieved the accuracy of  $R^2 = 0.73$  and  $RMSE = 0.115$ . This advancement over the conventional ocean-color algorithms is particularly significant for river-dominated coastal margins.

Third, compared with other CDOM inversion algorithms, the advantages of QAA-CDOM are as follows: 1) It does not require presetting prior parameters, such as specific chlorophyll absorption, and spectral slopes of CDOM and nonalgal particles; 2) it does not use the short wavelength band at 410 nm, which often has low signal-to-noise ratio; and 3) it is robust and fast and, hence, feasible for the inversion of a large amount of satellite images. In addition, all intermediate variables between  $R_{rs}$  and  $a_g(440)$  are examined in this study. Therefore, QAA-CDOM can be used to retrieve intermediate variables accurately, such as  $a_t(555)$ ,  $b_{bp}(440)$ , and  $a_p(440)$ . The derived  $a_p(440)$  can be further used to retrieve the optical properties of chlorophyll and nonalgal particles,  $a_{ph}(440)$  and  $a_d(440)$ , for example, using QAA's steps 7–10 [27].

Finally, the availability of hyperspectral and high-resolution satellite images opens a potential research area of using remote sensing to monitor the land–water dynamics associated with hydrological connectivity and estuarine processes. The advantages of using EO-1 Hyperion images (the best available spaceborne imaging spectrometer at 30-m resolution) are its narrow bands and spatial resolution. The narrow contiguous bands allow accurately locating the absorption or scattering wavelengths that are the most significant to the ocean-color components in coastal regions. Spatial resolution made it possible to

observe riverine CDOM distribution. However, it does require special attention for the facts that Hyperion short wavelength (440 nm) leads to some artifacts and uncertainties in the resultant  $a_g(440)$  images. We expect to test other hyperspectral sensors, which were reported to have better spectral quality at short wavelength, for example, the MERIS or Compact High Resolution Imaging Spectrometer—Project for On-Board Autonomy.

#### ACKNOWLEDGMENT

The authors would like to thank R. F. Chen and B. G. Gardner for their fieldtrip design, field data collection, and suggestions in data analysis. The authors would also like to thank W. Huang and K. Ciliano at the University of Massachusetts—Boston for processing discrete samples.

#### REFERENCES

- [1] N. B. Nelson and D. A. Siegel, "Chromophoric DOM in open ocean," in *Biochem. Marine Dissolved Organic Matter*, D. A. Hansell and C. A. Carlson, Eds. San Diego, CA: Academic Press, 2002, Ch. 11.
- [2] N. V. Blough, O. C. Zafriou, and J. Bonilla, "Optical-absorption spectra of waters from the Orinoco River outflow—Terrestrial input of colored organic-matter to the Caribbean," *J. Geophys. Res.*, vol. 98, no. C2, pp. 2271–2278, 1993.
- [3] C. E. Del Castillo, P. G. Coble, J. M. Morell, J. M. López, and J. E. Corredor, "Analysis of the optical properties of the Orinoco River plume by absorption and fluorescence spectroscopy," *Marine Chem.*, vol. 66, no. 1/2, pp. 35–51, Jul. 1999.
- [4] G. M. Ferrari, M. D. Dowell, S. Grossi, and C. Targa, "Relationship between the optical properties of chromophoric dissolved organic matter and total concentration of dissolved organic carbon in the southern Baltic Sea region," *Marine Chem.*, vol. 55, no. 3/4, pp. 299–316, Dec. 1996.
- [5] A. Vodacek, N. V. Blough, M. D. DeGrandpre, E. T. Peltzer, and R. K. Nelson, "Seasonal variation of CDOM and DOC in the Middle Atlantic Bight: Terrestrial inputs and photooxidation," *Limnol. Oceanogr.*, vol. 42, no. 2, pp. 674–686, Jun. 1997.
- [6] C. A. Stedmon, S. Markager, M. Sondergaard, T. Vang, A. Laubel, N. H. Borch, and A. Windelin, "Dissolved organic matter (DOM) export to a temperate estuary: Seasonal variations and implications of land use," *Estuaries Coasts*, vol. 29, no. 3, pp. 388–400, Jun. 2006.
- [7] N. B. Nelson, D. Siegel, and A. Michaels, "Seasonal dynamics of colored dissolved material in the Sargasso Sea," *Deep-Sea Res. Part I—Oceanogr. Res. Papers*, vol. 45, no. 6, pp. 931–957, Jun. 1998.
- [8] D. A. Siegel, A. F. Michaels, J. C. Sorensen, M. C. O'Brien, and M. A. Hammer, "Seasonal variability of light availability and utilization in the Sargasso Sea," *J. Geophys. Res.*, vol. 100, no. C5, pp. 8695–8713, May 1995.
- [9] P. A. Raymond and J. E. Bauer, "Riverine export of aged terrestrial organic matter to the North Atlantic Ocean," *Nature*, vol. 409, no. 6819, pp. 497–499, Jan. 2001.
- [10] C. Freeman, C. D. Evans, D. T. Monteith, B. Reynolds, and N. Fenner, "Export of organic carbon from peat soils," *Nature*, vol. 412, no. 6849, p. 785, Aug. 2001.
- [11] N. Roulet and T. R. Moore, "Browning the waters," *Nature*, vol. 444, no. 7117, pp. 283–284, Nov. 2006.
- [12] R. P. Bukata, J. H. Jerome, A. S. Kondratyev, and D. V. Pozdnyakov, *Optical Properties and Remote Sensing of Inland and Coastal Waters*. Boca Raton, FL: CRC Press, 1995.
- [13] K. L. Carder, F. R. Chen, Z. P. Lee, S. K. Hawes, and D. Kamykowski, "Semianalytic Moderate-Resolution Imaging Spectrometer algorithms for chlorophyll a and absorption with bio-optical domains based on nitrate-depletion temperatures," *J. Geophys. Res.*, vol. 104, no. C3, pp. 5403–5421, 1999.
- [14] S. A. Garver and D. A. Siegel, "Inherent optical property inversion of ocean color spectra and its biogeochemical interpretation 1. Time series from the Sargasso Sea," *J. Geophys. Res.*, vol. 102, no. C8, pp. 18 607–18 625, Aug. 1997.
- [15] J. E. O'Reilly, S. Maritorena, B. G. Mitchell, D. A. Siegel, K. L. Carder, S. A. Garver, M. Kahru, and C. McClain, "Ocean color chlorophyll algorithms for SeaWiFS," *J. Geophys. Res.*, vol. 103, no. C11, pp. 24 937–24 953, 1998.



- [16] V. E. Brando and A. G. Dekker, "Satellite hyperspectral remote sensing for estimating estuarine and coastal water quality," *IEEE Trans. Geosci. Remote Sens.*, vol. 41, no. 6, pp. 1378–1387, Jun. 2003.
- [17] D. D'Alimonte, G. Zibordi, and J.-F. Berthon, "Determination of CDOM and NPPM absorption coefficient spectra from coastal water remote sensing reflectance," *IEEE Trans. Geosci. Remote Sens.*, vol. 42, no. 8, pp. 1770–1777, Aug. 2004.
- [18] A. Mannino, M. E. Russ, and S. B. Hooker, "Algorithm development and validation for satellite-derived distributions of DOC and CDOM in the US Middle Atlantic Bight," *J. Geophys. Res.*, vol. 113, no. C7, pp. C07051–1–C07051–19, Jul. 2008.
- [19] M. Kahru and B. G. Mitchell, "Seasonal and nonseasonal variability of satellite-derived chlorophyll and colored dissolved organic matter concentration in the California current," *J. Geophys. Res.*, vol. 106, no. C2, pp. 2517–2529, 2001.
- [20] E. J. D'Sa and R. L. Miller, "Bio-optical properties in waters influenced by the Mississippi River during low flow conditions," *Remote Sens. Environ.*, vol. 84, no. 4, pp. 538–549, Apr. 2003.
- [21] A. Morel and B. Gentili, "A simple band ratio technique to quantify the colored dissolved and detrital organic material from ocean color remotely sensed data," *Remote Sens. Environ.*, vol. 113, no. 5, pp. 998–1011, May 2009.
- [22] Q. Yu, Y. Q. Tian, R. F. Chen, A. Liu, G. G. Bernard, and W. Zhu, "Functional linear analysis of in situ hyperspectral data for assessing CDOM in rivers," *Photogramm. Eng. Remote Sens.*, vol. 76, no. 10, pp. 1147–1158, Oct. 2010.
- [23] "Remote sensing of inherent optical properties: Fundamentals, tests of algorithms, and applications," IOCCG, Dartmouth, NS, Canada, 2006.
- [24] S. Maritorena, D. A. Siegel, and A. R. Peterson, "Optimization of a semi-analytical ocean color model for global-scale applications," *Appl. Opt.*, vol. 41, no. 15, pp. 2705–2714, May 2002.
- [25] F. E. Hoge and P. E. Lyon, "Satellite retrieval of inherent optical properties by linear matrix inversion of oceanic radiance models: An analysis of model and radiance measurement errors," *J. Geophys. Res.*, vol. 101, no. C7, pp. 16 631–16 648, Jul. 1996.
- [26] W. Yang, B. Matsushita, J. Chen, and T. Fukushima, "A relaxed matrix inversion method for retrieving water constituent concentrations in case II waters: The case of Lake Kasumigaura, Japan," *IEEE Trans. Geosci. Remote Sens.*, vol. 49, no. 9, pp. 3381–3392, Sep. 2011.
- [27] Z. P. Lee, K. L. Carder, and R. A. Arnone, "Deriving inherent optical properties from water color: A multiband quasi-analytical algorithm for optically deep waters," *Appl. Opt.*, vol. 41, no. 27, pp. 5755–5772, Sep. 2002.
- [28] C. F. Le, Y. M. Li, Y. Zha, D. Sun, and B. Yin, "Validation of a quasi-analytical algorithm for highly turbid eutrophic water of Meiliang Bay in Taihu Lake, China," *IEEE Trans. Geosci. Remote Sens.*, vol. 47, no. 8, pp. 2492–2500, Aug. 2009.
- [29] P. Shanmugam, "New models for retrieving and partitioning the colored dissolved organic matter in the global ocean: Implications for remote sensing," *Remote Sens. Environ.*, vol. 115, no. 6, pp. 1501–1521, Jun. 2011.
- [30] D. A. Siegel, S. Maritorena, N. B. Nelson, D. A. Hansell, and M. Lorenzi-Kayser, "Global distribution and dynamics of colored dissolved and detrital organic materials," *J. Geophys. Res.*, vol. 107, no. C12, pp. 3228–3242, 2002.
- [31] P. Kowalczyk, W. J. Cooper, R. F. Whitehead, M. J. Durako, and W. Sheldon, "Characterization of CDOM in an organic-rich river and surrounding coastal ocean in the South Atlantic Bight," *Aquatic Sci.*, vol. 65, no. 4, pp. 384–401, Dec. 2003.
- [32] R. L. Miller, C. E. Del Castillo, and B. A. McKee, *Remote Sensing of Coastal Aquatic Environments: Technologies, Techniques, and Applications*. New York: Springer-Verlag, 2005.
- [33] W. N. Zhu, "Inversion and analysis of chromophoric dissolved organic matter in estuarine and coastal regions using hyperspectral remote sensing," Ph.D. dissertation, Dept. Geosci., Univ. Massachusetts Amherst, Amherst, MA, 2011.
- [34] Y. Qin, V. E. Brando, A. G. Dekker, and D. Blondeau-Patissier, "Validity of SeaDAS water constituents retrieval algorithms in Australian tropical coastal waters," *Geophys. Res. Lett.*, vol. 34, no. L21, pp. L21603–1–L21603–4, Nov. 2007.
- [35] Z. P. Lee, A. Weidemann, J. Kindle, R. Arnone, K. L. Carder, and C. Davis, "Euphotic zone depth: Its derivation and implication to ocean-color remote sensing," *J. Geophys. Res.*, vol. 112, no. C3, pp. C03009–1–C03009–11, 2007.
- [36] W. N. Zhu, Q. Yu, Y. Q. Tian, R. F. Chen, and G. B. Gardner, "Estimation of chromophoric dissolved organic matter in the Mississippi and Atchafalaya River plume regions using above-surface hyperspectral remote sensing," *J. Geophys. Res.*, vol. 116, no. C2, pp. C02011–1–C02011–22, 2011.
- [37] UACE, *US Army Corps of Engineers—Atchafalaya Basin Project*, 2008. [Online]. Available: <http://www.mvn.usace.army.mil/pao/bro/AtchafalayaBasinProject.pdf>
- [38] R. F. Chen and G. B. Gardner, "High-resolution measurements of chromophoric dissolved organic matter in the Mississippi and Atchafalaya River plume regions," *Marine Chem.*, vol. 89, no. 1–4, pp. 103–125, Oct. 2004.
- [39] R. R. Lane, J. W. Day, B. Marx, E. Reves, and G. P. Kemp, "Seasonal and spatial water quality changes in the outflow plume of the Atchafalaya River, Louisiana, USA," *Estuaries*, vol. 25, no. 1, pp. 30–42, Feb. 2002.
- [40] J. D. Pakulski, R. Benner, T. Whittedge, R. Amon, B. Eadie, L. Cifuentes, J. Ammerman, and D. Stockwell, "Microbial metabolism and nutrient cycling in the Mississippi and Atchafalaya River plumes," *Estuarine Coastal Shelf Sci.*, vol. 50, no. 2, pp. 173–184, Feb. 2000.
- [41] R. F. Chen, "In situ fluorescence measurements in coastal waters," *Organic Geochem.*, vol. 30, no. 6, pp. 397–409, Jun. 1999.
- [42] R. F. Chen, P. Bissett, P. Coble, R. Conmy, G. B. Gardner, M. A. Moran, X. Wang, M. L. Wells, P. Whelan, and R. G. Zepp, "Chromophoric dissolved organic matter (CDOM) source characterization in the Louisiana Bight," *Marine Chem.*, vol. 89, no. 1–4, pp. 257–272, Oct. 2004.
- [43] S. W. Bailey and P. J. Werdell, "A multi-sensor approach for the on-orbit validation of ocean color satellite data products," *Remote Sens. Environ.*, vol. 102, no. 1, pp. 12–23, May 2006.
- [44] K. S. Khurshid, K. Staenz, L. Sun, R. Neville, H. P. White, A. Bannari, C. M. Champagne, and R. Hitchcock, "Preprocessing of EO-1 Hyperion data," *Can. J. Remote Sens.*, vol. 32, no. 2, pp. 84–97, Apr. 2006.
- [45] B. Datt, T. R. McVicar, T. G. Van Niel, D. L. B. Jupp, and J. S. Pearlman, "Preprocessing EO-1 Hyperion hyperspectral data to support the application of agricultural indexes," *IEEE Trans. Geosci. Remote Sens.*, vol. 41, no. 6, pp. 1246–1259, Jun. 2003.
- [46] T. Han, D. G. Goodenough, A. Dyk, and J. Love, "Detection and correction of abnormal pixels in Hyperion images," in *Proc. IEEE IGARSS*, Toronto, ON, Canada, 2002, pp. 1327–1330.
- [47] F. L. Gadallah, F. Csillag, and E. J. Smith, "Destriping multisensor imagery with moment matching," *Int. J. Remote Sens.*, vol. 21, no. 12, pp. 2505–2511, Aug. 2000.
- [48] L. X. Sun, R. Neville, K. Staenz, and H. P. White, "Automatic destriping of Hyperion imagery based on spectral moment matching," *Can. J. Remote Sens.*, vol. 34, no. S1, pp. S68–S81, May 2008.
- [49] G. W. Felde, G. P. Anderson, T. W. Cooley, M. W. Matthew, S. M. Adler-Golden, A. Berk, and J. Lee, "Analysis of Hyperion data with the FLAASH atmospheric correction algorithm," in *Proc. IGARSS*, 2003, vol. 1, pp. 90–92.
- [50] M. W. Matthew, S. M. Adler-Golden, A. Berk, G. W. Felde, G. P. Anderson, D. Gorodetzky, S. E. Paswaters, and M. Shippert, "Atmospheric correction of spectral imagery: Evaluation of the FLAASH algorithm with AVIRIS data," in *Proc. SPIE*, 2003, vol. 5093, pp. 474–482.
- [51] J. G. Yuan, Z. Niu, and X. P. Wang, "Atmospheric correction of Hyperion hyperspectral image based on FLAASH," *Spectr. Spectral Anal.*, vol. 29, no. 5, pp. 1181–1185, May 2009.
- [52] S. M. Adler-Golden, P. K. Acharya, A. Berk, M. W. Matthew, and D. Gorodetzky, "Remote bathymetry of the littoral zone from AVIRIS, LASH, and QuickBird imagery," *IEEE Trans. Geosci. Remote Sens.*, vol. 43, no. 2, pp. 337–347, Feb. 2005.
- [53] W. J. Moses, A. A. Gitelson, R. L. Perk, D. Gurlin, D. C. Rundquist, B. C. Leavitt, T. M. Barrow, and P. Brakhage, "Estimation of chlorophyll-a concentration in turbid productive waters using airborne hyperspectral data," *Water Res.*, vol. 46, no. 4, pp. 993–1004, Mar. 2012.
- [54] C. D. Mobley, "Estimation of the remote-sensing reflectance from above-surface measurements," *Appl. Opt.*, vol. 38, no. 36, pp. 7442–7455, Dec. 1999.
- [55] G. C. Chang and R. W. Gould, "Comparisons of optical properties of the coastal ocean derived from satellite ocean color and in situ measurements," *Opt. Exp.*, vol. 14, no. 22, pp. 10 149–10 163, Oct. 2006.
- [56] Z. P. Lee and K. L. Carder, "Absorption spectrum of phytoplankton pigments derived from hyperspectral remote-sensing reflectance," *Remote Sens. Environ.*, vol. 89, no. 3, pp. 361–368, Feb. 2004.
- [57] H. G. Zhan, S. Ping, and C. Chuqun, "A Bayesian based quasi-analytical algorithm for retrieval of inherent optical properties from ocean color," *Chin. Sci. Bull.*, vol. 50, no. 23, pp. 2770–2777, Dec. 2005.
- [58] M. Babin, A. Morel, V. Fournier-Sicre, F. Fell, and D. Stramski, "Light scattering properties of marine particles in coastal and open ocean waters as related to the particle mass concentration," *Limnol. Oceanogr.*, vol. 48, no. 2, pp. 843–859, 2003.



- [59] M. Babin, D. Stramski, G. M. Ferrari, H. Claustre, A. Bricaud, G. Obolensky, and N. Hoepffner, "Variations in the light absorption coefficients of phytoplankton, nonalgal particles, and dissolved organic matter in coastal waters around Europe," *J. Geophys. Res.*, vol. 108, no. C7, pp. 3211–3231, 2003.
- [60] D. L. B. Jupp, "Discussion around Hyperion data: Background notes for the Hyperion data users workshop," presented at the CSIRO Earth Observation Centre, Canberra, Australia, 2002.
- [61] J. T. O. Kirk, *Light and Photosynthesis in Aquatic Ecosystems*, 2nd ed. New York: Cambridge Univ. Press, 1994.
- [62] H. R. Gordon, O. B. Brown, R. H. Evans, J. W. Brown, R. C. Smith, K. S. Baker, and D. K. Clark, "A semianalytic radiance model of ocean color," *J. Geophys. Res.*, vol. 93, no. D9, pp. 10 909–10 924, Sep. 1988.
- [63] Z. P. Lee, K. L. Carder, C. D. Mobley, R. G. Steward, and J. S. Patch, "Hyperspectral remote sensing for shallow waters: 1. A semianalytical model," *Appl. Opt.*, vol. 37, no. 27, pp. 6329–6337, Sep. 1998.
- [64] Z. P. Lee, R. Arnone, C. Hu, P. J. Werdell, and B. Lubac, "Uncertainties of optical parameters and their propagations in an analytical ocean color inversion algorithm," *Appl. Opt.*, vol. 49, no. 3, pp. 369–381, Jan. 2010.
- [65] S. A. Green and N. V. Blough, "Optical-absorption and fluorescence properties of chromophoric dissolved organic-matter in natural-waters," *Limnol. Oceanogr.*, vol. 39, no. 8, pp. 1903–1916, Dec. 1994.
- [66] R. Del Vecchio and A. Subramaniam, "Influence of the Amazon River on the surface optical properties of the western tropical North Atlantic Ocean," *J. Geophys. Res.*, vol. 109, no. C11, pp. C11001-1–C11001-13, Nov. 2004.



**Weining Zhu** received the Ph.D. degree in geosciences from the University of Massachusetts, Amherst, in 2012.

He was with the Department of Geosciences, University of Massachusetts. He is currently a Postdoctoral Researcher with the Institute for Great Lakes Research and the Department of Geography, Central Michigan University, Mount Pleasant. His research focuses on ocean color, hyperspectral remote sensing, and Geographic Information Science spatial analysis.



**Qian Yu** received the B.S. and M.S. degrees in geography from Nanjing University, Nanjing, China, in 1999 and 2001, respectively, and the Ph.D. degree from the University of California, Berkeley, in 2005.

Since 2006, she has been with the Department of Geosciences, University of Massachusetts, Amherst. Her research focuses on hyperspectral and high-resolution remote sensing of vegetation and water biogeochemistry. She is also interested in remote-sensing-assisted modeling of watershed carbon cycle.